PAPER

# Effects of Electromagnet Interference on Speed and Position Estimations of Sensorless SPMSM

**Yuanhe XUE**[†], **Wei YAN**[†a)], **Xuan LIU**[†], **Mengxia ZHOU**[†], **Yang ZHAO**[†], *and* **Hao MA**[†], *Nonmembers*

**SUMMARY**    Model-based sensorless control of permanent magnet synchronous motor (PMSM) is promising for high-speed operation to estimate motor state, which is the speed and the position of the rotor, via electric signals of the stator, beside the inevitable fact that estimation accuracy is degraded by electromagnet interference (EMI) from switching devices of the converter. In this paper, the simulation system based on Luenberger observer and phase-locked loop (PLL) has been established, analyzing impacts of EMI on motor state estimations theoretically, exploring influences of EMI with different cutoff frequency, rated speeds, frequencies and amplitudes. The results show that Luenberger observer and PLL have strong immunity, which enable PMSM can still operate stably even under certain degrees of interference. EMI produces sideband harmonics that enlarge pulsation errors of speed and position estimations. Additionally, estimation errors are positively correlated with cutoff frequency of low-pass filter and the amplitude of EMI, and negatively correlated with rated speed of the motor and the frequency of EMI. When the frequency is too high, its effects on motor state estimations are negligible. This work contributes to the comprehensive understanding of how EMI affects motor state estimations, which further enhances practical application of sensorless PMSM.
*key words: permanent magnet synchronous machine (PMSM) drives, Luenberger observer, immunity, electromagnet interference (EMI), estimation errors*

## 1.  Introduction

Permanent magnet synchronous motor (Permanent magnet synchronous motor, PMSM) is attractive for transportation, aerospace, household and the other application [1]–[12] due to simple structure, reliable operation, fast response and high efficiency. To implement coordinate transformation and decoupling control in the field-oriented control of PMSM, information about the speed and the position of the rotor must be known [13]–[16]. However, information identified by the mechanical position sensor may cause some problems related to extended axial length, extra cost, reliability concern and operational environment. In order to solve these problems, the speed and the position are estimated by sensorless control techniques instead of the mechanical position sensor.

There are two main categories of sensorless control techniques for PMSM [13]–[16], including high frequency injection methods based on saliency tracking and back-electromotive force (back-EMF) methods based on machine model. Although injecting high frequency signals, such as rotating signals [17], pulsating vibration signals [9] and so

on, works well in zero and low speed range, may bring additional losses and more fluctuations in the torque ripple. Moreover, its application to nonsalient sensorless surface-mounted PMSM (SPMSM) is difficult. On the contrary, back-EMFs based on machine model for medium and high speed range is usually calculated by observers, such as Luenberger observer [2], [3], [18]–[20], Kalman observer [21]–[23], disturbance observer [24]–[28], sliding mode observer [1], [4]–[8], [11], [29]–[35] and so on [10]. Then, applying the inverse tangent function or phase-locked loop (PLL), the speed and the position are extracted from back-EMFs.

Nevertheless, speed and position estimations are always contaminated by numerous factors. One such factor is high-frequency chattering in traditional sliding mode observer. To suppress estimation errors aroused by the chattering, discontinuous sign function is replaced by continuous functions as sliding mode surface [1], [5]–[8], [11], [30], [32], [34], [35], to further adapt various operating conditions, and gain coefficients of sliding mode surface are online optimized by the fuzzy control or a back-propagation neural network [1], [11], [30]. For another example, when the rotor is reversed, position error of $\pi$ is generated by conventional PLL. [2]–[4] proposed new PLL to identify exact rotor position in both forward and backward directions. Speed and position estimations are also influenced by magnetic field distribution and inverter nonlinearity. [31], [32] pointed that the two factors cause $6k \pm 1$ harmonic components in the stator current and estimated back-EMFs, resulting in $6k$ harmonic components in estimation errors of speed and position. Likewise, it is a considerable factor that direct current bias of the detecting process of current and voltage sensors in real-time estimations [27], [33]. In addition, considering load torque disturbance, [22], [25], [28], [35] proposed a voltage feedforward compensation method to improve estimation precision. [20] developed the model of the observer in the Laplace domain to investigate the effects of multiple factors, including phase delay of observer's response, current measurement noise, voltage actuation distortion and parameter uncertainty.

From previous research, many domestic and abroad scholars have involved in research on motor state estimations affected by inverter nonlinearity, magnetic field of permanent magnet, the detecting process, PLL or the observer, except electromagnet interference (EMI) from switching devices of the converter. Especially, when switching frequency is high, EMI makes the stator currents distort, performed as "spikes" of the waveform in the time domain and a large amount of

high-frequency harmonics in the frequency domain. This can disturb speed and position estimations, leading to speed fluctuations, mechanical vibrations and noise pollution. Different from former research, new contribution of this paper is concluded as follows: 1) quantificationally analyzing effects of EMI on motor state estimation in sensorless SPMSM, relationship expressions between EMI, back-EMF errors and estimation errors of speed and position are derived; 2) the controlled variable method is employed to explore EMI with different cutoff frequency, rated speeds, frequencies and amplitudes.

The organization of this paper is as follows: in Sect. 2, to simplify the analyses, adopting a classic Luenberger linear observer, the method to estimate speed and position is proposed; Sect. 3 introduces EMI model into the sensorless SPMSM system; Sect. 4 conducts comparative simulations to verify; Finally, the conclusions are listed in Sect. 5.

## 2. Sensorless PMSM Control Strategy

It is assumed that a three-phase PMSM is an ideal motor, motor currents regarded as symmetrical three-phase sine waves, ignoring the saturation of the motor iron core and disregarding eddy currents and hysteresis losses. The mathematic model of SPMSM can be written as current state equation in the $\alpha\beta$ stationary reference frame as

$$\begin{cases} \dfrac{di_\alpha}{dt} = -\dfrac{R_S}{L_S}i_\alpha + \dfrac{1}{L_S}u_\alpha - \dfrac{1}{L_S}e_\alpha \\ \dfrac{di_\beta}{dt} = -\dfrac{R_S}{L_S}i_\beta + \dfrac{1}{L_S}u_\beta - \dfrac{1}{L_S}e_\beta \end{cases} \quad (1)$$

where $R_S$ and $L_S$ are stator resistance and inductance, respectively, $i_\alpha, i_\beta$ and $u_\alpha, u_\beta$ are $\alpha\beta$-axis currents and voltages, respectively, and $e_\alpha$ and $e_\beta$ are $\alpha\beta$-axis actual back-EMFs, also expressed as

$$\begin{cases} e_\alpha = -e\sin\theta_e = -\omega_e\lambda_f\sin\theta_e \\ e_\beta = -e\cos\theta_e = \omega_e\lambda_f\cos\theta_e \end{cases} \quad (2)$$

where $e = \omega_e\psi_f$ denotes motor back-EMF and $\psi_f$ is the rotor flux linkage generated by permanent magnet. $\omega_e$ and $\theta_e$ are the speed and the position of the rotor, respectively, representing motor state.

The mathematic model of SPMSM can be written as mechanic state equation in the $dq$ rotating reference frame as

$$\frac{1}{p}\theta_e = -\frac{F}{J}\frac{\omega_e}{p} + \frac{3}{2}\frac{p\psi_f}{J}i_q - \frac{T_N}{J} \quad (3)$$

where $p$ is pole number, $J$ is inertia, $F$ is viscous damping, $T_N$ is load torque, and $i_q$ is $dq$-axis currents, also expressed as

$$i_q = -i_\alpha\sin\theta_e + i_\beta\cos\theta_e \quad (4)$$

The design of Luenberger observer in PMSM depending on the difference between the real system and the observer's system, estimated back-EMFs of the motor is calculated by reconstructing internal state of the observer's system [13]–[15]. The model of Luenberger observer can be
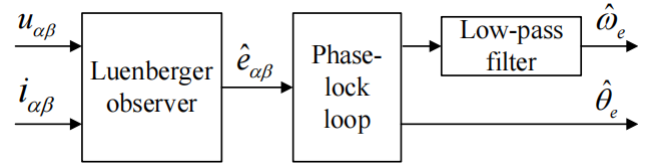


**Fig. 1** Block diagram of speed and position estimations

written in the $\alpha\beta$ stationary reference frame as

$$\begin{cases} \dfrac{d\hat{i}_\alpha}{dt} = -\dfrac{R_S}{L_S}\hat{i}_\alpha - \dfrac{1}{L_S}\hat{e}_\alpha + \dfrac{1}{L_S}u_\alpha + k_1\tilde{i}_\alpha \\ \dfrac{d\hat{i}_\beta}{dt} = -\dfrac{R_S}{L_S}\hat{i}_\beta - \dfrac{1}{L_S}\hat{e}_\beta + \dfrac{1}{L_S}u_\beta + k_1\tilde{i}_\beta \\ \dfrac{d\hat{e}_\alpha}{dt} = -\omega_e\hat{e}_\beta + k_2\tilde{i}_\alpha \\ \dfrac{d\hat{e}_\beta}{dt} = \omega_e\hat{e}_\alpha + k_2\tilde{i}_\beta \end{cases} \quad (5)$$

where $k_1$ and $k_2$ are observer coefficients, $\wedge$ denotes estimated values, and $\sim$ denotes estimation errors, $\tilde{i}_\alpha = \hat{i}_\alpha - i_\alpha$, $\tilde{i}_\beta = \hat{i}_\beta - i_\beta$.

By manipulation of (1) and (5), it is possible to acquire transfer function linking estimated back-EMF and actual back-EMF

$$\frac{\hat{e}}{e} = \frac{-k_2}{(s - j\omega_e)(sL_S + R_s + k_1L_s) - k_2} \quad (6)$$

In terms of (2), back-EMF contain information about speed and position, which extracted by PLL are more precise than those extracted by the inverse tangent function, the structure of entire estimation system depicted in Fig. 1.

## 3. Speed and Position Estimation Modeling Based on Electromagnetic Interference

In a three-phase circuit, current sensors are installed in Phase A and B. According to Kirchhoff's current law, The mathematic model of EMI can be expressed in the three-phase reference frame as

$$\begin{cases} i_a = i'_a + \Delta i_a \\ i_b = i'_b + \Delta i_b \\ i_c = -i_a - i_b \end{cases} \quad (7)$$

where $i_a$, $i_b$ and $i_c$ are three-phase currents that are subsequently used to estimate the speed and the position, $i'_a$, $i'_b$ and $i'_c$ are actual currents without EMI, $i_a = I\sin(\omega_e + \varphi_a)$, $i_b = I\sin(\omega_e + \varphi_a - 2\pi/3)$, and $\Delta i_a$ and $\Delta i_b$ are current errors induced by EMI. Clarke's matrix transforms (7) to the form in the $\alpha\beta$ stationary reference frame as

$$\begin{cases} i_\alpha = i'_\alpha + \Delta i_\alpha \\ i_\beta = i'_\beta + \Delta i_\beta \end{cases} \quad (8)$$

where $i'_\alpha$ and $i'_\beta$ are $\alpha\beta$-axis actual currents without EMI, $i_\alpha = I\sin(\omega_e + \varphi_a)$, $i_\beta = -I\cos(\omega_e + \varphi_a)$, and $\Delta i_\alpha$ and $\Delta i_\beta$ are $\alpha\beta$-axis current errors induced by EMI, also expressed
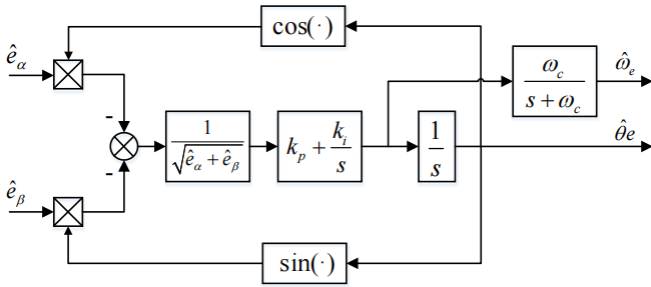
**Fig. 2** Block diagram of the PLL

as

$$\begin{cases} \Delta i_\alpha = \Delta i_a \\ \Delta i_\beta = \dfrac{\sqrt{3}}{3}\Delta i_a + \dfrac{2\sqrt{3}}{3}\Delta i_b \, . \end{cases} \tag{9}$$

Luenberger observer, as a strict linear system, conforms to superposition theorem. Hence, estimated back-EMFs are separated into two parts

$$\begin{cases} \hat{e}_\alpha = e_\alpha + \Delta e_\alpha \\ \hat{e}_\beta = e_\beta + \Delta e_\beta \end{cases} \tag{10}$$

where $e_\alpha$ and $e_\beta$ are regarded as one part, $\Delta e_\alpha$ and $\Delta e_\beta$ are $\alpha\beta$-axis back-EMF errors regarded as the other part. They are responsive to actual currents and current errors, respectively. (6) can be rearranged yielding an expression for estimated back-EMFs

$$\begin{cases} \Delta \hat{e}_\alpha = \dfrac{-k_2}{(s - j\omega_e)(sL_s + R_s + k_1L_s) - k_2} \\ \qquad \cdot (-R_s\Delta i_\alpha - sL_s\Delta i_\alpha) \\ \Delta \hat{e}_\beta = \dfrac{-k_2}{(s - j\omega_e)(sL_s + R_s + k_1L_s) - k_2} \\ \qquad \cdot (-R_s\Delta i_\beta - sL_s\Delta i_\beta) \end{cases} \tag{11}$$

Considering that the amplitudes of back-EMFs varies under diverse operating conditions, normalization which makes the amplitude lose the dimension is incorporated into PLL, reducing complexity and computational burden of the system, removing mismatches of the amplitudes. The entire scheme of PLL with the heterodyning and the normalization is depicted in Fig. 2.

In Fig. 2, $k_i$ and $k_p$ are the integration coefficient and the proportional coefficient, respectively. $\dfrac{\omega_c}{s + \omega_c}$ and $\dfrac{1}{s}$ represent low-pass filter and integrator, respectively, which both can inhibit high-frequency signals. $\omega_c$ is cutoff frequency of low-pass filter. $\Delta\theta_e$ is error between estimated position and actual position

$$\Delta\theta_e = \frac{-(\hat{e}_\alpha)\cos\hat{\theta}_e - (\hat{e}_\beta)\sin\hat{\theta}_e}{\sqrt{\hat{e}_\alpha^2 + \hat{e}_\beta^2}}. \tag{12}$$

Substituting (2) and (10) into (12), position error can be rewritten as

$$\begin{aligned} \Delta\theta_e &= \frac{e}{|\hat{e}|}\sin(\theta_e - \hat{\theta}_e) \\ &\quad - \frac{1}{|\hat{e}|}\left[\Delta e_\beta \sin\hat{\theta}_e + \Delta e_\alpha \cos\hat{\theta}_e\right] \\ &\approx \frac{e}{|\hat{e}|}(\theta_e - \hat{\theta}_e) - \frac{\Delta e}{|\hat{e}|}\sin(\hat{\theta}_e + \varphi) \end{aligned} \tag{13}$$

where $\varphi = \arctan(\Delta e_\alpha / \Delta e_\beta)$ denotes the phase, $\Delta\omega_e$ is speed error obtained by differentiation

$$\Delta\omega_e = \frac{d(\Delta\theta_e)}{dt}. \tag{14}$$

On the right side of (13), the first term is estimation error induced by the estimation algorithm itself, while the second term is estimation error induced by EMI. Through the aforementioned derivations, it is inferred that EMI can enlarge estimation errors of speed and position. What's more, the greater the magnitude of $|\Delta e|$ induced by EMI, the larger estimation errors are.

According to sinusoidal steady state law, if the angular frequency of $\Delta i$ is $\omega_{\Delta_i}$, the angular frequency of output response in Luenberger observer will be $\omega_{\Delta_i}$, too. Thus, estimated back-EMF assumed as $\Delta e = A_e \cdot \sin(\omega_{\Delta_i} + \varphi_{\Delta_e})$, the second term in (13) is rewritten as

$$\begin{aligned} &\frac{\Delta e}{|\hat{e}|}\sin\left(\hat{\theta}_e + \varphi\right) \\ &= \frac{\Delta e}{|\hat{e}|}\sin\left(\hat{\omega}_e t + \varphi\right) \\ &= \frac{A}{|\hat{e}|}\left\{\cos\left[(\omega_{\Delta i} - \hat{\omega}_e)t + \varphi_{\Delta e} - \varphi\right]\right. \\ &\qquad \left. - \cos\left[(\omega_{\Delta i} + \hat{\omega}_e)t + \varphi_{\Delta e} + \varphi\right]\right\} \end{aligned} \tag{15}$$

It is inferred that EMI signal with angular frequency of $\omega_{\Delta_e}$ can cause harmonic ripples whose angular frequencies are $\omega_{\Delta_i} - \omega_e$ and $\omega_{\Delta_i} + \omega_e$ in estimation errors of the speed and the position.

Combined (2), the second term in (13) is also rewritten as

$$\frac{\Delta e}{|\hat{e}|}\sin(\hat{\theta}_e + \varphi) = \frac{\Delta e}{\omega_e\psi_f + |\Delta e|}\sin(\hat{\theta}_e + \varphi). \tag{16}$$

It is inferred that estimation errors of the speed and the position induced by EMI become smaller as $\omega_e$ increases.

## 4. Case Study and Result Analysis

### 4.1 Settings of Cases

Figure 3 displays a universal strategy of sensorless SPMSM control, the system adopting double closed-loop regulations of the speed and the current, as well as field-oriented control of $i_d = 0$. The modulation mode of the inverter is space vector pulse width modulation (SVPWM). On the basis of Sect. 2, actual speed and position are obtained via mechanic parameters of mathematic model of SPMSM, while estimated speed and position are obtained via electrical parameters of the model of Luenberger observer. Mechanic
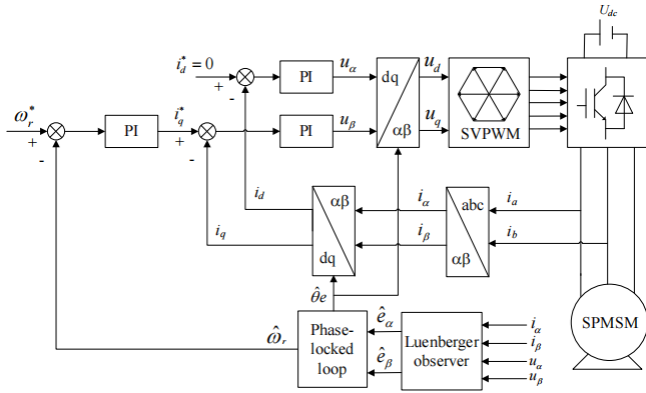
**Fig. 3**    Block diagram of sensorless control system

**Table 1**    SPMSM system parameters.

| Symbol | Quantity | Value |
|--------|----------|-------|
| $R_S$ | stator resistance | $0.11\ \Omega$ |
| $L_s$ | stator inductance | $0.97\ \text{mH}$ |
| $\Psi_f$ | flux linkage | $0.1119\ \text{Wb}$ |
| $p$ | pole number | 4 |
| $J$ | inertia | $1.6\ \text{g}\cdot\text{m}^2$ |
| $F$ | viscous damping | $0.2024\ \text{N}\cdot\text{mm}\cdot\text{s}$ |
| $T_N$ | load torque | $10\ \text{N}\cdot\text{m}$ |

and electrical parameters, illustrated in Table 1, are one kind of common SPMSM. Simulation parameters set as variable step, the algorithm is ode45 and the relative error is 0.001.

### 4.2    Speed and Position Estimations with EMI

Working state of the motor are reflected in Fig. 4. Setting cutoff frequency to 200 Hz, a sine wave of $20\cdot\sin(2\pi\cdot10\cdot10^3\cdot t)$ mA was artificially imposed into the motor as an EMI signal, when the time is 0.7 s.

Waveforms about estimated speed and actual speed, as shown in Fig. 4 (a), speed error between estimated speed and actual speed, as shown in Fig. 4 (b), no matter whether there is EMI or not, estimated speed and actual speed both rise and fall around the rated speed of $\omega_r^* = 3000\pi\ \text{min}^{-1}$. Before interference is imposed, estimated speed fluctuates between $2999\pi$ and $3000.8\pi\ \text{min}^{-1}$, while the approximate range of speed error is $\pm2.6\pi\ \text{min}^{-1}$. After interference is imposed, estimated error fluctuates between $2993.6\pi$ and $3006.4\pi\ \text{min}^{-1}$, while the approximate range of speed error goes up to $\pm7.6\pi\ \text{min}^{-1}$.

Signals about the position are a zigzag wave whose value domain is from 0 to $2\pi$. When the electrical angle is equal to $2\pi$, it will become 0. As shown in Fig. 4 (c), estimated position (blue solid line) is almost coincident with actual position (red solid line). To better distinguish their difference, position error between estimated position and actual position is as shown in Fig. 4 (d). Before interference is imposed, the approximate range of position error is $\pm0.002$ rad. After interference is imposed, the approximate range of position error grows up to $\pm0.0075$ rad.
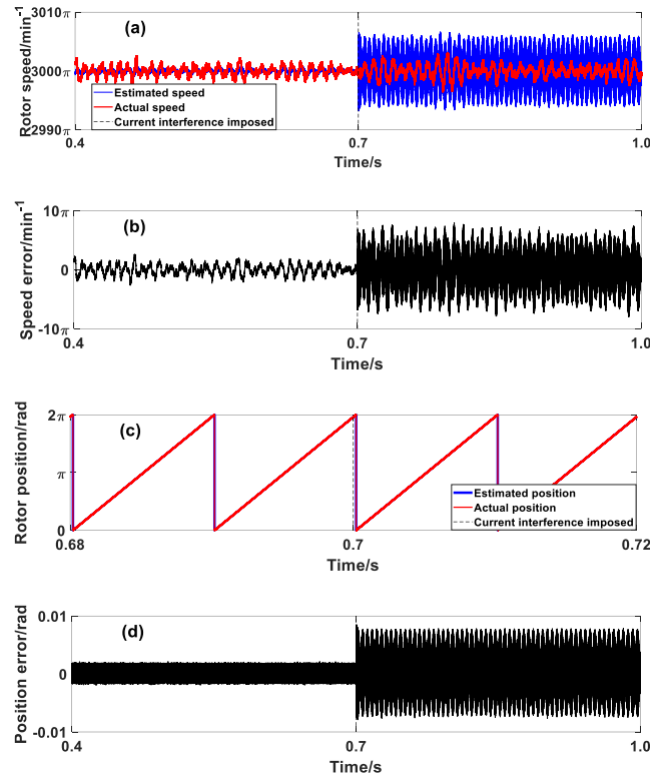


**Fig. 4**    Effects of EMI on motor state estimations
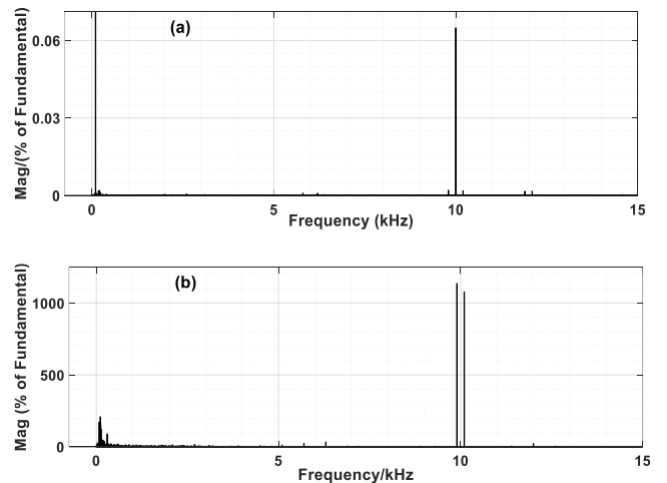


**Fig. 5**    Block diagram of sensorless control system

Figure 5 shows components in frequency domain of estimated $\alpha$-axis back-EMF and speed error conducted by fast Fourier transform. The frequency of EMI is 10 kHz, which results in a peak in the spectrum of back-EMF at this frequency, as shown in Fig. 5 (a), due to the same frequency response produced by Longberg observer. Furthermore, since the rated speed of $3000\pi\ \text{min}^{-1}$ is equivalent to a frequency of 100 Hz, spectral peaks of speed error appear at $10^4 \pm 100$ Hz, as depicted in Fig. 5 (b). This result is in agreement with the derivation of (15).

It can be seen that the sensorless control system based
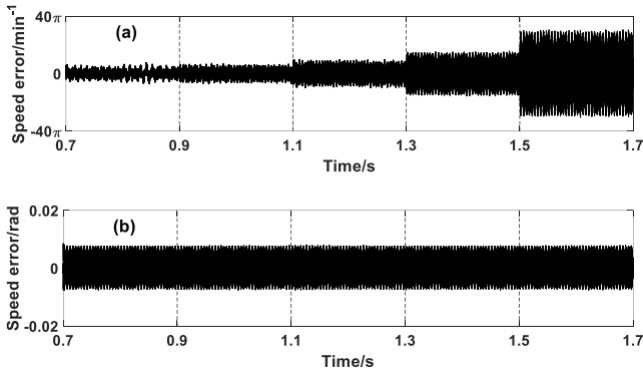
**Fig. 6** Effects of EMI with different cutoff frequency on motor state estimations



**Fig. 7** Effects of EMI with different rated speeds on motor state estimations

on Luenberger observer and PLL has strong anti-interference capability, as it can still provide accurate estimation of PMSM state even when EMI happens. However, estimation accuracy is deteriorated by EMI, which enlarges fluctuation ranges of speed and position estimations, generating harmonic ripple at the sideband near the frequency of EMI.

### 4.3 Effects with Different Cutoff Frequency of Low-Pass Filter

In order to investigate the effect of EMI on speed error under different cutoff frequency, ensuring the EMI signal and rated speed remained unchanged, cutoff frequency of low-pass filter are 150 Hz at 0.7~0.9 s, 200 Hz at 0.9~1.1 s, 300 Hz at 1.1~1.3 s, 500 Hz at 1.3~1.5 s, and 1000 Hz at 1.5~1.7 s, respectively. Speed error, as shown in Fig. 6 (b), corresponding approximate ranges are $\pm 7.4\pi$, $\pm 7.6\pi$, $\pm 9.8\pi$, $\pm 15.6\pi$, $\pm 30.4\pi$ min$^{-1}$, respectively, while position error, as shown in Fig. 6 (b), corresponding approximate ranges all are $\pm 0.0075$ rad.

It can be seen that low-pass filter inhibits high-frequency interference of speed error, without altering position error. The lower cutoff frequency, the smaller speed error. Not that lower cutoff frequency is better. When cutoff frequency is too low, the system response will increase, and even useful information about estimated speed may be filtered out. Thus, it's crucial to weigh the value of cutoff frequency.

### 4.4 Effects with Different Rated Speeds of the Motor

In order to investigate the effect of EMI on motor state estimation under different operating conditions, ensuring the EMI signal and cutoff frequency remained unchanged, the initial value of rated speed is set as $4000\pi$ min$^{-1}$, and the motor is decelerated at 0.7~0.8 s, 1.1~1.2 s, and 1.5~1.6 s, respectively, with rated speed dropping to $3000\pi$, $2000\pi$ and $1000\pi$ min$^{-1}$, while rated speeds are a constant at the rest time.

Figure 7 (a) shows estimated speed, which can track the rated speed. Position errors and speed errors are as shown in Fig. 7 (b) and 7 (c), respectively. During the period of the deceleration, a direct current bias exists in both errors, and during the beginning stages of deceleration and constant speed, there is a dramatic overshoot oscillation in both errors. Upon reaching a steady-state, approximate ranges of speed error for rated speeds $\omega_r{}^* = 4000\pi$, $3000\pi$, $2000\pi$, and $1000\pi$ min$^{-1}$ are $\pm 6.2\pi$, $\pm 7.6\pi$, $\pm 10\pi$, and $\pm 19.6\pi$ min$^{-1}$, respectively, while approximate ranges of position errors for these speeds are $\pm 0.0066$, $\pm 0.0075$, $\pm 0.01$, and $\pm 0.019$ rad, respectively.
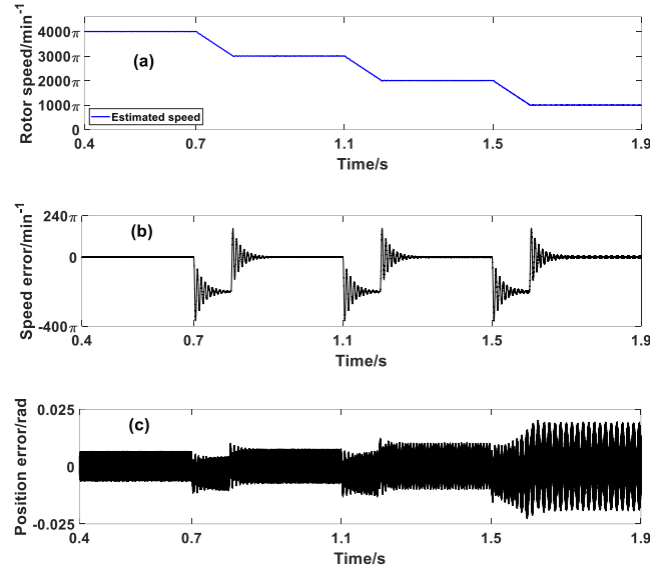
It can be seen that the sensorless control system based on Luenberger observer and PLL has adaptive capability to changes of the rated speed. Speed errors and position errors induced by EMI will rise up, as rated speed decreases. This conclusion is in agreement with the derivation of (16).

### 4.5 Effects with EMI of Different Amplitudes and Frequencies

Considering EMI with different amplitudes and frequencies, their simulations are carried out separately in the following.

Ensuring the frequency of the EMI, rated speed of the motor and cutoff frequency remained unchanged ($f = 10$ kHz, $\omega_r{}^* = 3000\pi$ min$^{-1}$, $\omega_c = 200$ Hz), the amplitudes of the EMI are 0 at 0.4~0.6 s, 5 mA at 0.6~0.8 s, 10 mA at 0.8~1.0 s, 20 mA at 1.0~1.2 s, 40 mA at 1.2~1.4 s, and 60 mA at 1.4~1.6 s, respectively. Particularly, the amplitude of 0 at 0.4~0.6 s represents the control group, which means there is no EMI. Speed error, as shown in Fig. 8 (a), corresponding approximate ranges are $\pm 2.6\pi$, $\pm 5.4\pi$, $\pm 6\pi$, $\pm 7.6\pi$, $\pm 11\pi$, $\pm 13.6\pi$ min$^{-1}$, respectively, while position error, as shown in Fig. 8 (b), corresponding approximate ranges are $\pm 0.002$, $\pm 0.0032$, $\pm 0.0047$, $\pm 0.0075$, $\pm 0.013$, $\pm 0.019$ rad, respectively.

Ensuring the amplitude of the EMI and rated speed of the motor remained unchanged ($I = 20$ mA, $\omega_r{}^* =$
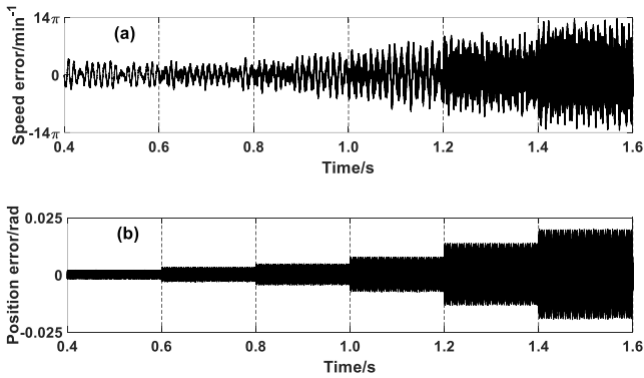
**Fig. 8** Effects of EMI with different amplitudes on motor state estimations
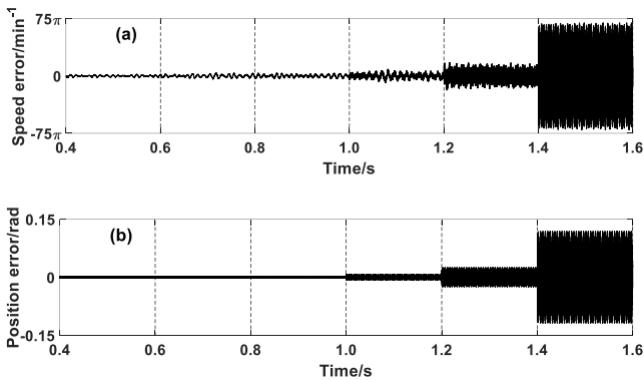


**Fig. 9** Effects of EMI with different frequencies on motor state estimations



**Fig. 10** Bode diagram of Luenberger observer
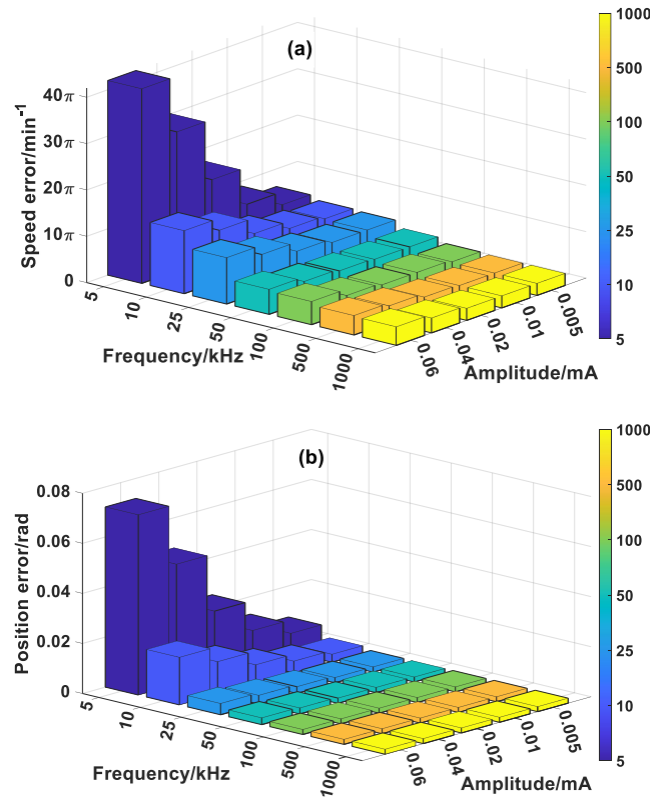


**Fig. 11** Effects of EMI with different amplitudes and frequencies on motor state estimations

$3000\pi \, \mathrm{min}^{-1}$, $\omega_c = 200\,\mathrm{Hz}$). The frequencies of the EMI are 50 kHz at 0.6~0.8 s, 25 kHz at 0.8~1.0 s, 10 kHz at 1.0~1.2 s, 5 kHz at 1.2~1.4 s, and 2.5 kHz at 1.4~1.6 s, respectively. Likewise, the situation without EMI at 0.4~0.6 s represents the control group. Speed error, as shown in Fig. 9 (a), corresponding approximate ranges are $\pm 2.6\pi$, $\pm 4\pi$, $\pm 6\pi$, $\pm 7.6\pi$, $\pm 17\pi$, $\pm 70\pi \, \mathrm{min}^{-1}$, respectively, while position error, as shown in Fig. 9 (b), corresponding approximate ranges are $\pm 0.002$, $\pm 0.0021$, $\pm 0.0027$, $\pm 0.0075$, $\pm 0.025$, $\pm 0.11$ rad, respectively. Among them, speed error and position error at 25 and 50 kHz are almost the same as those without EMI. Since Luenberger observer possesses a filter characteristic, the high-frequency interference is filtered out. Bode diagram of the observer as described in Fig. 10, the higher the frequency of EMI, the severer the attenuation of EMI.

In order to research effects of EMI more comprehensively, different combinations of amplitudes and frequencies are tested, and approximate ranges of speed errors and position errors is statistically as shown in Fig. 11 (a) and 11 (b), respectively. The column height represents absolute value of approximate range of speed error or position error, the higher the column, the larger the error. The column color represents the frequency of EMI. If the colors are identical, the frequencies of EMI are identical.

According to the columns, it can be seen that speed errors and position errors both rise up as the amplitude of EMI increases, while both errors go down as the frequency of EMI increases. However, when the frequency overs 50 kHz, the both errors no longer changes with the change of the amplitude. Effects of EMI with high-frequency on the motor state estimation can be ignored, this highlighting the strong anti-interference in sensorless control systems again.

From typical point, EMI as a common problem in electronic system, leads to stator current errors at first, and subsequently current errors flowing into Luenberger observer causes back-EMF error. Finally, estimation errors of speed and position are induced by back-EMF error through PLL.

## 5.  Conclusion

This paper reveals coupling mechanism between EMI and sensorless PMSM control, and simulation results are consistent with the theoretical conclusions.  Results conclude that sensorless PMSM control, consisting of Luenberger observer and PLL, has strong immunity.  Additionally, EMI produces sideband harmonics and enlarges pulsation errors of speed and position estimations, which are positively correlated with cutoff frequency of low-pass filter and the amplitude of EMI, and negatively correlated with the rated speed of the motor and the frequency of EMI. When the frequency is too high, its effects on motor state estimations are negligible. Of course, there are still a few limitations to the proposed research. In zero and low speed range, Luenberger observer, like other observers, cannot estimate back-EMFs.  Furthermore, (2) is invalid for interior PMSM (IPMSM), because its direct inductance is not equal to quadrature inductance.  Thus, the application in this paper is just to SPMSM in medium and high speed range.  After all, there are discrepancies between simulations and realities.  An experimental platform will be performed to further verify conclusions in the future.

## Acknowledgments

### References

[1]  Y. Wang, J. Wu, Z. Guo, C. Xie, J. Liu, and X. Jin, "Flux-weakening fuzzy adaptive ST-SMO sensorless control algorithm for PMSM in EV," The Journal of Supercomputing, vol.78, no.8, pp.10930–10949, Feb. 2022.

[2]  Q. Zeng adn Y. Chen, "Sensorless control for PMSM in underwater propeller based on improved phase-locked loop," IEICE Electron. Express, vol.18, no.11, pp.1–6, June 2021.

[3]  Y. Chen, Q. Zeng, X. Dai, W. Wu, and H. Li, "Sensorless control of PMSM used by underwater propulsion based on new phase-locked loop," Chinese Journal of Electron Devices, vol.44, no.5, pp.1090–1097, Oct. 2021.

[4]  D. Xu, L. Yang, H. Wu, Y. Yuan, and F. He, "An improved PLL sensorless PMSM rotor position estimation method for EV," Journal of Guizhou University (Natural Sciences), vol.36, no.4, pp.54–58, Aug. 2019.

[5]  F. Du, F. Xu, and X. Wu, "PMSM speed sensorless system of intercity railway track inspection trolley based on FOSMO-MRAS observer," Journal of Physics: Conference Series, vol.2395, no.1, pp.54–58, Dec. 2022.

[6]  X. Xiao, Y. Zhang, J. Wang, and H. Du, "New adaptive sliding-mode observer design for sensorless control of PMSM in electric vehicle drive system," International Journal on Smart Sensing and Intelligent Systems, vol.9, no.1, pp.377–396, Jan. 2016.

[7]  H. Bai, J. Zhu, and J. Qin, "Improved SMO based sensorless PMSM vector control in ship electric propulsion system," Navigation of China, vol.38, no.4, pp.22–25, Dec. 2015.

[8]  Y. Zhang, "Sensorless control of PMSM for washing machine based on improved SMO," Light Industry Machinery, vol.33, no.4, pp.44–47+53, Aug. 2015.

[9]  O. Kechiche, H. Sethom, H. Sammoud, and I. Belkhodja, "Optimized high frequency signal injection based permanent magnet synchronous motor rotor position estimation applied to washing machines," American Journal of Engineering and Applied Sciences, vol.4, no.3, pp.390–399, Sept. 2011.

[10]  S. Murshid, and B. Singh, "Energy-efficient single-stage solar PV powered sensorless PMSM drive for water pumping," IET Renewable Power Generation, vol.13, no.13, pp.2267–2277, Oct. 2019.

[11]  L. Sheng, W. Li, Y. Wang, M. Fan, and X. Yang, "Sensorless Control of a Shearer Short-Range Cutting Interior Permanent Magnet Synchronous Motor Based on a New Sliding Mode Observer," IEEE Access, vol.5, no.1, pp.18439–18450, Aug. 2017.

[12]  S. Singh, S. Singh, and A. Tiwari, "PMSM drives and its application: an overview," Recent Advances in Electrical & Electronic Engineering, vol.16, no.1, pp.4–16, Sept. 2023.

[13]  L. Sheng, L. Liu, and Q. Ye, "Status and prospect on no position sensor control of permanent magnet synchronous motor," Electrotechnics Electric, vol.302, no.2, pp.1–8, Feb. 2023.

[14]  S. Singh, A. Tiwari, and S. Singh, "Speed and position estimation for sensorless control of PMSM: a critical review," Recent Advances in Electrical & Electronic Engineering, vol.13, no.6, pp.804–822, Nov. 2020.

[15]  Q. Wang, S. Wang, and C. Chen, "Review of sensorless control techniques for PMSM drives," IEEJ Transactions on Electrical and Electronic Engineering, vol.14, no.10, pp.1543–1552, July 2019.

[16]  J. Liu, F. Xiao, Y. Shen, Z. Mai, and C. Li, "Position-sensorless control technology of permanent-magnet synchronous motor-a review," Transactions of China Electrotechnical Society, vol.32, no.16, pp.76–88, Aug. 2017.

[17]  E. Li, X. Zhang, H. Li, and S. Yang, "Research on improved IPMSM position detection based on rotated high frequency injection," Power Electronics, vol.53, no.7, pp.36–38, July 2019.

[18]  X. Huang, P. Guan, H. Pan, S. Liu, G. Du, X. Huang, and X. Wang, "Research on grey predictive control of PMSM based on reduced-order Luenberger observer," Journal of Electrical Engineering & Technology, vol.16, no.5, pp.2635–2646, June 2021.

[19]  Y. Zhu, B. Tao, M. Xiao, G. Yang, X. Zhang, and K. Lu, "Luenberger position observer based on deadbeat-current predictive control for sensorless PMSM," Electronics, vol.9, no.8, pp.1325–1341, July 2020.

[20]  S. Bolognani, S. Calligaro, and R. Petrella, "Design issues and estimation errors analysis of back-EMF-based position and speed observer for SPM synchronous motors," IEEE Journal of Emerging and Selected Topics in Power Electronics, vol.2, no.2, pp.159–170, June 2014.

[21]  H. Shu, C. Guo, Y. Song, X. Chen, and S. Luo. "Design of model predictive controllers for PMSM drive system based on the extended Kalman filter observer," International Journal of Electric and Hybrid Vehicles, vol.11, no.4, pp.378–394, Jan. 2019.

[22]  Z. He, W. Ding, H. Xiao, M. Zou, L. XU, Z. Xie, L. Zhu, and W. Bao, "Inertia Compensation for Permanent Magnet Synchronous Motors Based on Extended Kalman Filter," Journal of Hunan University of Technology, vol.33, no.6, pp.8–14, Nov. 2019.

[23]  T. Shi, Z. Wang, and C. Xia, "Speed measurement error suppression for PMSM control system using self-adaption Kalman observer," IEEE Trans. Ind. Electron., vol.62, no.5, pp.2753–2763, May 2015.

[24]  Y. Zhang, Z. Wu, Q. Yan, N. Huang, and G. Du, "An improved model-free current predictive control of permanent magnet synchronous motor based on high-gain disturbance observer," Energies, vol.16, no.1, pp.141–156, Dec. 2022.

[25]  X. Liu, and H. Yu, "Continuous adaptive integral-type sliding mode control based on disturbance observer for PMSM drives," Nonlinear Dynamics, vol.104, no.2, pp.1429–1441, March 2021.

[26]  B. Sarsembayev, K. Suleimenov, and T.D. Do, "High order disturbance observer based PI-PI control system with tracking anti-windup technique for improvement of transient performance of PMSM," IEEE Access, vol.9, no.1, pp.66323–66334, April 2021.

[27] D. Xiao, S. Nalakath, Y. Sun, J. Wiseman, and A. Emadi, "Complex-coefficient adaptive disturbance observer for position estimation of IPMSMs with robustness to DC errors," IEEE Trans. Ind. Electron., vol.67, no.7, pp.5924–5935, July 2020.

[28] X. Lu, H. Lin, and J. Han, "Load disturbance observer-based control method for sensorless PMSM drive," IET Electric Power Applications, vol.10, no.8, pp.378–394, Sept. 2016.

[29] X. Lu, H. Lin, Y. Feng, and J. Han, "Soft switching sliding mode observer for PMSM sensorless control," Transactions of China Electrotechnical Society, vol.30, no.2, pp.106–113, Jan. 2015.

[30] G. Wang, and H. Zhang, "A second-order sliding mode observer optimized by neural network for speed and position estimation of PMSMs," Journal of Electrical Engineering & Technology, vol.17, no.1, pp.415–423, Jan. 2022.

[31] X. Song, J. Fang, B. Han, and S. Zheng, "Adaptive compensation method for high-speed surface PMSM sensorless drives of EMF-based position estimation error," IEEE Trans. Power Electron., vol.31, no.2, pp.1438–1449, Feb. 2016.

[32] G. Zhang, G. Wang, D. Xu, and N. Zhao, "ADALINE-network-based PLL for position sensorless interior permanent magnet synchronous motor drives," IEEE Trans. Power Electron., vol.31, no.2, pp.1450–1460, April 2015.

[33] Y. Wang, Y. Xu, and J. Zou, "ILC based voltage compensation method for PMSM sensorless control considering inverter nonlinearity and sampling current DC bias," IEEE Trans. Ind. Electron., vol.67, no.7, pp.5980–5989, July 2020.

[34] W. Kang, and H. Li, "Improved sliding mode observer based sensorless control for PMSM," IEICE Electron. Express, vol.14, no.24, pp.1–6, Nov. 2017.

[35] Y. Liu, and X. Wang, "Speed global integral sliding mode control with a load sliding mode observer for PMSM," IEICE Electron. Express, vol.15, no.6, pp.1–12, March 2017.

**Xuan Liu** was born in China. In 2018, He graduated from Anhui Polytechnic University, in Wuhu, China, with a bachelor's degree in engineering. He is a master student at Nanjing Normal University with research interests in electromagnetic compatibility and PM machines control.



**Mengxia Zhou** received the M.S. degree in electrical engineering and the Ph.D. degree in physics and electronics from Nanjing Normal University, in 2018 and 2021, respectively. His main research interests include electromagnetic compatibility and high frequency device modeling.



**Yang Zhao** is a Doctor & Professor from Nanjing Normal University. He received the M.S. degree and the Ph.D. degree in power electronics from Nanjing University of Aeronautics and Astronautics, in 1992 and 1995, respectively. His main research interests include electromagnetic compatibility and power electronics.



**Hao Ma** was born in China. In 2019, He graduated from Jiangsu Normal University, in Xuzhou, China, with a bachelor's degree in engineering. He is a master student at Nanjing Normal University with research interests in electromagnetic compatibility and PM machines control.



**Yuanhe Xue** was born in China. In 2020, he graduated from East China Jiaotong University in Nanchang, China, majoring in electrical engineering and automation, with a master's degree in engineering. He is a doctor student at Nanjing Normal University with research interests in electromagnetic compatibility and PM machines control.



**Wei Yan** is a Doctor & Assoc. Professor from Nanjing Normal University. He obtained the Physics and Electronics Ph.D. and Electrical Engineering M.S. from Nanjing Normal University in 2014 and 2011. He is the Senior Member of China Electrical Technology Association and the evaluation expert of the Electromagnetic Compatibility Calibration Specification of China.